Regulatory element in fibrin triggers tension-activated transition from catch to slip bonds

Rustem I. Litvinov[a,b,1], Olga Kononova[c,d,1,2], Artem Zhmurov[d,e], Kenneth A. Marx[c], Valeri Barsegov[c,d,3], D. Thirumalai[f], and John W. Weisel[a,3]

[a]Department of Cell and Developmental Biology, University of Pennsylvania Perelman School of Medicine, Philadelphia, PA 19104; [b]Institute of Fundamental Medicine and Biology, Kazan Federal University, Kazan 420008, Russian Federation; [c]Department of Chemistry, University of Massachusetts Lowell, Lowell, MA 01854; [d]Laboratory of Computer and Mathematical Modeling of Biological Systems, Moscow Institute of Physics and Technology, Moscow Region 141700, Russian Federation; [e]Laboratory of Mathematical Modeling in Medicine, Sechenov University, Moscow 119991, Russian Federation; and [f]Department of Chemistry, University of Texas at Austin, Austin, TX 78712

Edited by Attila Szabo, National Institutes of Health, Bethesda, MD, and approved June 28, 2018 (received for review February 13, 2018)

Fibrin formation and mechanical stability are essential in thrombosis and hemostasis. To reveal how mechanical load impacts fibrin, we carried out optical trap-based single-molecule forced unbinding experiments. The strength of noncovalent A:a knob-hole bond stabilizing fibrin polymers first increases with tensile force (catch bonds) and then decreases with force when the force exceeds a critical value (slip bonds). To provide the structural basis of catch–slip-bond behavior, we analyzed crystal structures and performed molecular modeling of A:a knob-hole complex. The movable flap (residues γ295 to γ305) containing the weak calcium-binding site γ2 serves as a tension sensor. Flap dissociation from the B domain in the γ-nodule and translocation to knob 'A' triggers hole 'a' closure, resulting in the increase of binding affinity and prolonged bond lifetimes. The discovery of biphasic kinetics of knob-hole bond rupture is quantitatively explained by using a theory, formulated in terms of structural transitions in the binding pocket between the low-affinity (slip) and high-affinity (catch) states. We provide a general framework to understand the mechanical response of protein pairs capable of tension-induced remodeling of their association interface. Strengthening of the A:a knob-hole bonds at 30- to 40-pN forces might favor formation of nascent fibrin clots subject to hydrodynamic shear in vivo.

catch-slip bond | fibrin polymerization | fluctuating bottleneck | interface remodeling | GPU computing

Fibrin is the end product of blood clotting that constitutes a proteinaceous network providing the filamentous mechanical scaffold of clots and thrombi. Formation of fibrin is essential for stopping bleeding (hemostasis) and thrombotic obstruction of blood vessels (thrombosis). Fibrinogen is enzymatically converted to monomeric fibrin with exposed binding sites (knobs) 'A' and 'B' that interact with complementary sites (holes) 'a' and 'b' in the γ- and β-nodules, respectively, of the lateral D regions of another fibrin molecule (Fig. 1 *A*–*C*) (1). Fibrin polymerizes to form fibrin protofibrils, which elongate and aggregate into insoluble fibers that branch to form the space-filling network (Fig. 1 *A*–*C*). Mechanical stability of blood clots, in response to forces exerted, for example, by the blood flow and contracting platelets, is determined by the strength of the knob-hole interactions before covalent cross-linking. Binding of knobs 'A' to holes 'a' is necessary for fibrin polymerization (1). A:a knob-hole interactions govern formation of fibrin and influence the structure and properties of clots and thrombi.

We explored single-molecule forced rupture of A:a knob-hole bonds (5, 6). We discovered that the strength of A:a knob-hole bonds increases with tensile force up to $f \approx 30$–35 pN (catch bond), the nature of which is unknown in this context, and then decreases with force at $f > 35$ pN (slip bonds). A counterintuitive catch–slip bond behavior has been found in a number of systems—for example, P-selectin and PSGL-1 (7), E-cadherin dimer (8), integrin $\alpha5\beta1$ and fibronectin (9), bacterial adhesin FimH (10), von Willebrand factor and receptor GP1b (11, 12), kinetochore–microtubule attachments (13), microtubule–dynein complexes (14), and vinculin–F-actin linkage (15). The catch–slip bonds have been studied theoretically, including the two-state model (16, 17), sliding–rebinding model (18), hydrogen-bond network model (19), and other models (20). However, the structural basis of the catch–slip duality has eluded detailed characterization.

Here, we combined single-molecule forced unbinding assays in vitro and in silico to resolve the structural mechanism of the dual catch–slip response of fibrin polymers to tension (Fig. 1*G*). Dynamic restructuring of the A:a association interface was revealed, which results in formation of bound states with tension-dependent binding affinity, a requirement for the bond lifetime increase upon force application (16, 17). We provided a structure-based interpretation of the catch–slip dynamics for important interactions in fibrin (Fig. 1). We developed a theory by extending Zwanzig's fluctuating bottleneck (FB) model (21), introduced in the context of small-molecule binding to myoglobin, to quantitatively explain the experiments.

Significance

The fibrin network is the scaffold of blood clots that prevent bleeding. Fibrin formation is driven by noncovalent "knob-hole" bonds that determine the mechanical properties of clots. Counterintuitively, the strength of knob-hole bonds first increased (catch bond) and then decreased (slip bond) with tensile force, thereby displaying a rare dual catch–slip behavior. We resolved the structural mechanism of tension-activated strengthening of the knob-hole bond. Our theory quantitatively accounts for the biphasic catch–slip force response, which comprises an important aspect of fibrin structural bionanomechanics. The shear-enhanced strengthening of noncovalent knob-hole bonds might favor fibrin polymerization under blood flow and might prevent breakup of nascent blood clots in the circulation.

Author contributions: R.I.L., O.K., V.B., and J.W.W. designed research; R.I.L. and J.W.W. designed the experiment; O.K. and V.B. designed simulations; R.I.L. performed the experiment; O.K. performed simulations; O.K., V.B., and D.T. developed the model; R.I.L., O.K., A.Z., K.A.M., and V.B. analyzed data; and R.I.L., O.K., A.Z., K.A.M., V.B., D.T., and J.W.W. wrote the paper.

The authors declare no conflict of interest.

This article is a PNAS Direct Submission.

[1]R.I.L. and O.K contributed equally to this work.

[2]Present address: Department of Materials Science and Engineering, University of California, Berkeley, CA 94720.

[3]To whom correspondence may be addressed. Email: weisel@pennmedicine.upenn.edu or valeri_barsegov@uml.edu.

This article contains supporting information online at www.pnas.org/lookup/suppl/doi:10.1073/pnas.1802576115/-/DCSupplemental.

Published online August 7, 2018.

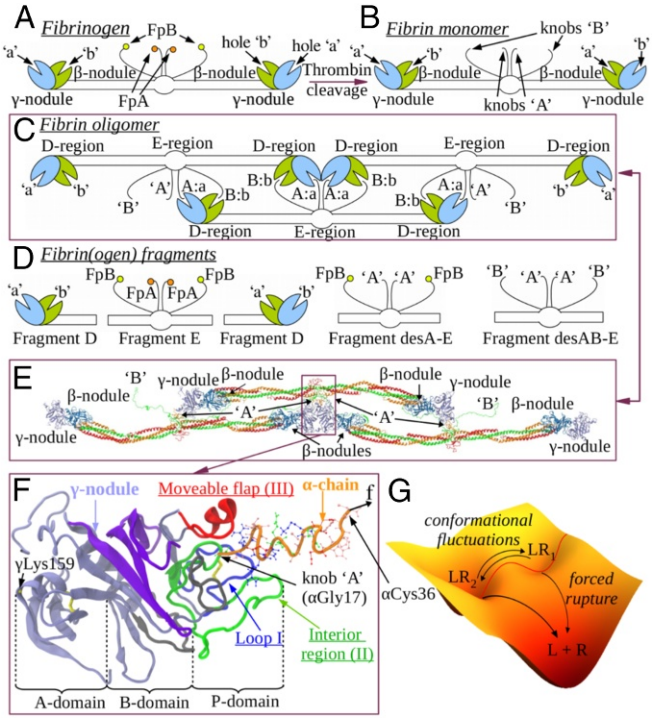

Fig. 1. Major steps and main structural determinants in fibrin polymerization. (*A–C*) Cleavage by thrombin of the fibrinopeptides A and B (FpA and FpB) in fibrinogen (*A*) converts it into fibrin with exposed knobs 'A' and 'B' (*B*), which bind to hole 'a' in the γ-nodules (blue) and 'b' in the β-nodule (green), facilitating fibrin oligomerization (*C*). (*D*) Fibrin fragments used in dynamic force assays in vitro and in silico. (*E*) Atomic model of a fibrin oligomer fragment (2) with the α-, β-, and γ-chains colored in orange, green, and red, respectively. The β- and γ-nodules are in light blue and light gray, respectively. (*F*) A:a knob-hole complex containing the γ-nodule with hole 'a' and the N-terminal part of the α-chain with knob 'A' (orange); hole 'a' is formed by domains A, B, and P (3); the three-stranded β-sheets stack in B domain is shown in purple. Loop I (blue), interior region (green), and movable flap (red) interact with knob 'A' (4). In simulations, the tensile force was applied to αCys36, and γLys159 was constrained. (*G*) Schematic of the energy landscape for A:a knob-hole interactions. Tension perturbs the equilibrium $LR_1 \leftrightarrow LR_2$ between the low-affinity bound state LR_1 and force-stabilized high-affinity bound state LR_2 changing the kinetics of forced rupture, $LR_{1,2} \rightarrow L + R$.

Results

A:a Knob-Hole Bond Dissociation Under Tensile Force.

Fibrin–fibrinogen bond lifetime as a function of constant tensile force. The A:a knob-hole interactions were probed at an interface during repeated touching of two microbeads coated covalently with fibrinogen (Fg), a source of holes 'a,' or monomeric fibrin (Fn), a source of knobs 'A' (*SI Appendix,* Fig. S1). By touching the Fn-coated surface with the Fg-coated surface, we allowed these molecules to form the A:a knob-hole complex (binding phase). Next, the surfaces were retracted by applying a constant tensile force to dissociate the A:a knob-hole bond (unbinding phase). Repeating the binding–unbinding cycles, we measured the lifetimes of Fg:Fn bonds, from which the force (f)-dependence of A:a knob-hole bond lifetimes was obtained (*SI Appendix,* Fig. S2*A*). The distributions of bond lifetimes $P(t;f)$ were collected for f=10–60 pN (*SI Appendix,* Fig. S3). These were used to calculate the average bond lifetimes $\langle\tau\rangle$, which first increased with f up to f= 30–35 pN and then decreased for $f > 40$ pN (Fig. 2*A*). Importantly, the addition of 3 mM $CaCl_2$ weakened the A:a bond, and the nonmonotonic dependence of $\langle\tau\rangle$ on f disappeared (Fig. 2*A*).

To distinguish the A:a binding from other interactions, we performed control experiments. Nonspecific surface-to-surface adhesion showed signals with $\tau < 0.03$ s. Specificity was tested by coating the surfaces with proteins lacking knobs and holes [bovine serum albumin (BSA)] or lacking knobs 'A' and 'B' (Fg). The control interactions (Fg/BSA, Fn/BSA, and Fg/Fg interfaces) revealed mostly (93–97%) short-lived signals with $\tau <$ 0.03 s and a small fraction (0.6–2.5%) of more stable interactions lasting 0.04–0.5 s (*SI Appendix,* Table S1). The bond lifetimes of control background interactions did not show dependence on force (Fig. 2*A*). To distinguish the A:a binding from other associations, we measured the Fg–Fn interaction in the absence/presence of the GPRPam peptide (knob 'A' inhibitor). GPRPam suppressed specific A:a knob-hole interactions lasting >0.5 s (*SI Appendix,* Fig. S2*A*). The binding probability for these interactions was several fold higher in the Fg–Fn system than in control systems, including Fg–Fn interactions inhibited by GPRP (*SI Appendix,* Fig. S2*A* and Table S1).

To test whether the intermediately strong interactions with 0.03 s $< \tau <$ 0.5 s contribute to the observed dependence of $\langle\tau\rangle$ on f, we also compared the bond lifetimes obtained either by including or excluding these intermediate-strength interactions to or from the datasets. The profiles of $\langle\tau\rangle$ (*SI Appendix,* Fig. S2*C*) and the cumulative binding probability vs. f (*SI Appendix,* Fig. S2*D*) were similar with a corresponding small shift to shorter bond lifetimes (*SI Appendix,* Fig. S2*D*) and to a higher binding probability (*SI Appendix,* Fig. S2*C*). We concluded that the bond lifetimes $\tau > 0.5$ s represented specific Fg–Fn or A:a knob-hole interactions. We included these data in subsequent analyses and modeling and discarded the bond lifetimes $\tau < 0.5$ s.

Bond lifetimes of the D:E complex as a function of tensile force. To minimize the role of nonspecific interactions due to the large size of full-length Fn/Fg molecules, we replaced Fg with its smaller proteolytic fragment D, containing the globular portion (with hole 'a') and Fn with fragment E comprising the central globule. Fragment E exists in three variants: (*i*) bearing both knobs 'A' and 'B' upon cleavage of fibrinopeptides A and B with thrombin (fragment desAB-E); (*ii*) bearing only knobs 'A' upon cleavage of fibrinopeptide A with batroxobin (fragment desA-E); and (*iii*) having no knobs if uncleaved (fragment E) (Fig. 1*D*). Specific interactions between fragments D and desAB-E also displayed the catch–slip character with $\langle\tau\rangle$ increasing with f up to $f = 30$–40 pN and then decreasing for $f > 40$ pN (Fig. 2*B*). The bell-like curve of $\langle\tau\rangle$ was quite similar to that for the Fg:Fn interactions (Fig. 2*B*), but with shorter average bond-lifetimes. The dual catch–slip behavior was largely suppressed with the addition of GPRP (*SI Appendix,* Fig. S2*E*), and it disappeared

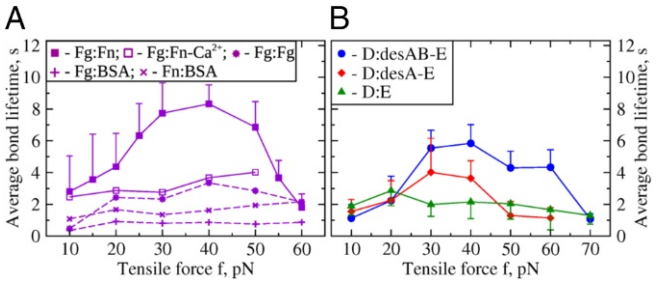

Fig. 2. Kinetics of rupture of A:a knob-hole bonds from single-molecule experiments. (*A*) Average bond lifetime $\langle\tau\rangle$ vs. force f for Fg:Fn interactions without and with Ca^{2+} (3 mM) and for control protein pairs both lacking knobs 'A' (Fg:Fg) or one of interacting proteins (BSA) or lacking knobs 'A' and holes 'a' (Fg:BSA and Fn:BSA). (*B*) $\langle\tau\rangle$ (>0.5 s) vs. f for fragment D (holes 'a' and 'b') coupled to fragments desAB-E (knobs 'A' and 'B') or desA-E (knob 'A'), or E (no knobs).

following a substantial reduction in surface density of fragment D (*SI Appendix*, Fig. S2*F*). These results indicate that the D/desAB-E interactions are specific and that they reflect formation–dissociation of the knob-hole bonds. Exposure of knob 'A' in fragment desA-E (without knob 'B') preserved its ability to interact with fragment D in the catch–slip fashion (Fig. 2*B*). The intact fragment E with uncleaved fibrinopeptides A and B was nonreactive with fragment D (Fig. 2*B*). This provides evidence that the interactions between fragment D and fragments desAB-E and desA-E are specific, and they reflected the A:a knob-hole bonds. Hence, the observed catch–slip behavior was due to specific A:a knob-hole interactions.

Molecular Modeling of A:a Knob-Hole Interactions.

Dynamic force measurements in silico. Inspired by our experimental findings, we performed simulations using ramped force $f(t)$ (*Materials and Methods*) and the atomic structural model of A:a knob-hole complex (Fig. 1*E*). Two unbinding scenarios characterized by faster vs. slower dissociation at lower vs. higher molecular force F were observed (*SI Appendix*, Fig. S4 *A* and *B*). For the pulling speed $\nu_f = 10^3$ μm/s, the A:a bonds ruptured at $F \approx 60$ pN in 50% of the 10 simulation runs and at 90 pN in 30% of runs, while in the remaining 20% of trajectories, the bonds dissociated at $F \approx 70$ pN (*SI Appendix*, Fig. S4*A*). For $\nu_f = 10^4$ μm/s, the bonds yielded at $F \approx 90$ and 130 pN in 70% and 30% of the 10 trajectories, respectively (*SI Appendix*, Fig. S4*B*). Hence, force stabilizes an alternative bound state not populated at $f = 0$.

Structural basis for the catch bond. We monitored the total number of persistent binding contacts, Q, between the residues in hole 'a' and knob 'A' as a function of time t. Q is a measure of binding affinity reflecting instantaneous changes in the bond strength. We also analyzed the maps of knob-hole contacts (residues γSer240–γLys380; *SI Appendix*, Fig. S5 *C* and *D*). We found that, unlike the bond rupture from the low-affinity bound state LR_1 (L, ligand; R, receptor), the structures accessed along the dissociation from the high-affinity bound state LR_2 were stabilized by force, which is linked to the origin of prolonged lifetimes (catch bond).

We characterized conformational transitions in hole 'a' under tension. Fig. 3 shows the profiles of F and Q and structures of the A:a knob-hole complex accessed along dissociation from the bound states LR_1 and LR_2. The $LR_1 \rightarrow LR_2$ transition is controlled by the movable flap, which serves as a tension-sensitive regulatory element triggering the opening/closing of the binding interface (snapshots 2a and 2b in Fig. 3). When negatively charged γAsp291, γAsp294, γAsp297, and γAsp301 in the movable flap interacted with positively charged γArg256 and γArg275 of the β-sheet stack in the B domain (*SI Appendix*, Fig. S5*C*), the binding interface was open (low-affinity bound state LR_1) and dissociation of knob 'A' was rapid (snapshots 2a in Fig. 3); see also an increase in contact density between the movable flap and B domain in *SI Appendix*, Fig. S5*C*. Under tension, the movable flap extended and translocated toward the ligand, thereby forming additional binding contacts between residues γAsp297–γPhe304 in the flap and αGly17–αGlu22 in knob 'A', which stabilized the high-affinity bound state LR_2 (snapshot 2b in Fig. 3). This triggered loop I straightening, leading to formation of additional binding contacts between residues γLys321–γGlu323 in loop I and residues αGlu22–αHis24 in knob 'A' (*SI Appendix*, Fig. S5*D*). As a result, the hole 'a' closed.

Movable flap is a mechanical nanoswitch. To elucidate the role of the movable flap, we performed simulations with constant force $f = 30$ pN. We correlated the dynamics of binding contacts between knob 'A' and the entire binding interface, Q, with the dynamics of contacts between knob 'A' and the movable flap, Q_{MF}. The observed nonmonotonic behavior of Q and Q_{MF} was due to the tilting back and forth of

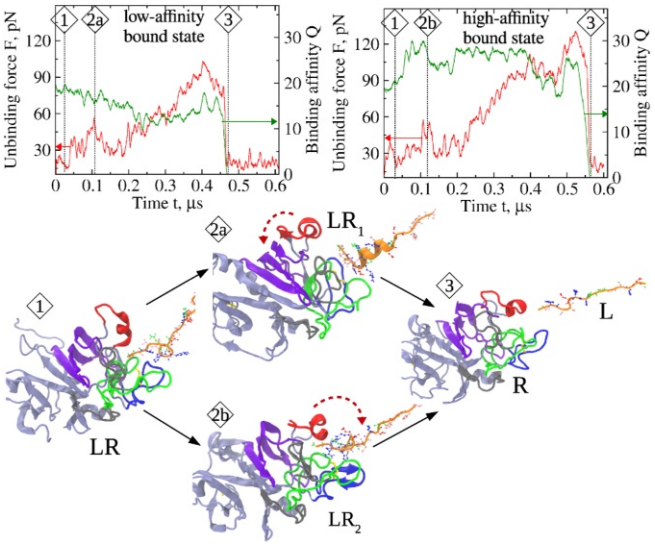

Fig. 3. Interface remodeling and forced rupture of the A:a knob-hole complex. (*Upper*) Profiles of rupture force F (red) and binding affinity Q (green) vs. time t from the force-ramp simulations. Rupture from state LR_1/LR_2 is characterized by lower/higher values of F and monotonic/nonmonotonic evolution of Q. (*Lower*) Snapshots 1–3 show the progress of rupture from the native state (structure 1) through intermediate state (structures 2a and 2b) and to dissociated state (structure 3). Low-affinity bound state LR_1: The movable flap interacts with the β-sheet stack of B domain (red arrow in structure 2a). High-affinity bound state LR_2: The movable flap moves to and catches knob 'A' (red arrow in structure 2b).

the movable flap (*SI Appendix*, Fig. S5*B*). This resulted in the flap switching on and off interactions with the β-sheet stack of the B domain. Additional binding contacts between residues in the movable flap and knob 'A' formed under tension (γPro299–αVal20, γSer300–αGly17, γSer300–αPro18, γAsp301–αArg19, γLys302–αGlu22, γPhe303–αPro18, γPhe303–αTrp33, and γPhe304–αVal20) were essential for the enhanced strength of the A:a bond at higher forces (Fig. 3). We quantified the flap elongation D_{MF} by measuring the distance between the flap and the β-sheet stack of the B domain (*SI Appendix*, Fig. S5*B*). We selected three pairs of residues in the movable flap and β-sheet stack: γGly296–γAla282, γAsp297–γGly283, and γAsp298–γGly284. For each pair, we calculated D_{MF} as a function of force and correlated changes in D_{MF} and in Q. The increase in Q from 15–20 to 25–30 was accompanied by a ∼1.5-fold increase in D_{MF} from 1.5 to 2.3 nm, which corresponded to the movable flap translocation from the periphery to the knob 'A' (*SI Appendix*, Fig. S5*B*). The decrease in Q from 25 to 17 was correlated with the decrease in D_{MF} from 2.3 to 1.3 nm, which corresponded to the flap tilting back (*SI Appendix*, Fig. S5*D*). Hence, the binding affinity increase (state LR_2) and the flap translocation were positively correlated (Fig. 3).

Analysis of Crystal Structures.

Movable flap and weak Ca-binding site γ2. We analyzed all 27 crystal structures of the γ nodule of human fibrin(ogen) (table S1 in ref. 2). In seven structures, Ca^{2+} is in the low-affinity Ca-binding site γ2 (22) coordinated by residues γAsp294, γGly296, γAsp298, and γAsp301 in the movable flap. The structures of hole 'a' with and without Ca^{2+} in γ2, overlaid in Fig. 4*E*, revealed significant structural changes upon calcium binding: γAsp297 and γAsp301 rotated away from knob 'A', forming contact with Ca^{2+}. Hence, the X-ray data indicated that Ca-binding to γ2 blocked the movable flap motion, which might suppress the catch-bond formation. This agreed well with the absence of any

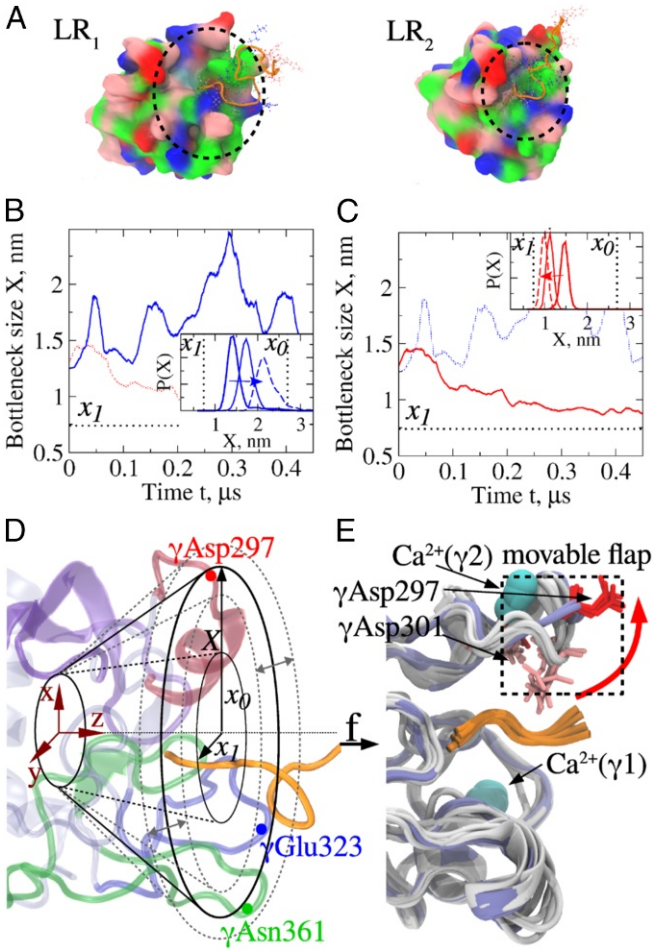

Fig. 4. Structural basis of the FB model of A:a bond rupture. (*A*) Snapshots of the A:a knob-hole complex with hole 'a' open (low-affinity state LR_1) and closed (high-affinity state LR_2). (*B* and *C*) The interface width X from two representative simulation runs, which resulted in bond rupture from state LR_1 (*B*) and LR_2 (*C*). *B* and *C*, *Insets* show probability distribution $P(X)$, sampled over a 0.1-μs time window. The shift of $P(X)$ over time (shown by arrows) reveals the continuous evolution of X. (*D*) Hole 'a' modeled as a FB of width X defined to be the radius of a circle circumscribing the triangle formed by residues γAsp297, γGlu323, and γAsn361. Under tension, X decreases from x_0 (LR_1) to x_1 (LR_2), which makes the rupture rate K depend on X. (*E*) Crystal structures of hole 'a' in the γ-nodule with (gray-blue) and without Ca^{2+} (gray) in the γ2 binding site in the movable flap (boxed) and the GPRP-terminal part of knob 'A' (orange). Upon binding of Ca^{2+} (cyan ball), γAsp297 in the movable flap rotates by 70° and shifts by 5 Å away from the GPRP-peptide (terminal part of knob 'A'; red arrow). Also shown is γAsp301 mutated to His in recombinant Fg Finland P21.

catch-bond regime in the Fg:Fn bond rupture kinetics in 3 mM $CaCl_2$ solution (Fig. 2).

Fluctuating Bottleneck Theory.

A:a interface remodeling. We analyzed the evolution in interface width X, defined as the radius of cross-sectional area formed by residues γAsp297, γGlu323, and γAsn361 in the movable flap, loop I, and interior region, respectively (Fig. 4). In state LR_1, X fluctuated between 1.3 and 2.5 nm (open hole 'a'; Fig. 4*B*); in state LR_2, X decreased from 1.3 to 0.8 nm (Fig. 4*C*), implying that the bottleneck is formed when hole 'a' closes. The profiles of distribution $P(X,t)$ (Fig. 4 *B* and *C*), corresponding to the evolutions of X, shifted to larger X (rupture from LR_1) or smaller X (from LR_2). Hence, hole 'a' was a bottleneck (21, 23–25) with tension-dependent width X.

Hole 'a' is a fluctuating bottleneck. Force affects the dynamics of hole 'a' closure and the kinetics of knob-A escape. The bond lifetime t and bottleneck width X are coupled random variables (Fig. 4*E*), described by the Smoluchowski equation for the joint distribution, $\frac{dP(X,t)}{dt}=[\mathbf{L}(X,t)-K(X)]P(X,t)$ (*SI Appendix*, Eq. S7), where the rate $K(X)=kX^2$ depending on rate constant $k(f)=k_0\exp[\sigma_y f/k_BT]$ (26) (k_0-attempt frequency and σ_y-transition distance for rupture) represents the kinetics of knob 'A' escape from the bottleneck, and in the operator $\mathbf{L}(X;t)=\frac{\partial}{\partial X}\left[\frac{\kappa}{\zeta}(X-\langle X\rangle)+\frac{k_BT}{\zeta}\frac{\partial}{\partial X}\right]$ the first and second terms describe tension dependence and fluctuations of X, respectively (ζ-friction coefficient). This equation can be solved as described in *SI Appendix* to obtain the Green's function solution $G(X,X_0;t)$. The distribution of bond lifetimes is $P(t)=\int_0^\infty dX\int_0^\infty dX_0\,G(X,X_0;t)P(X_0)$, and the average bond lifetime is $\langle\tau\rangle=\int_0^\infty dtP(t)t$. However, the millisecond timescale of bottleneck fluctuations ($\eta=\zeta/\kappa$; κ-interface stiffness) is much shorter than the bond lifetimes, and the initial distribution $P(X_0)=\delta(X_0-x_0)$ is peaked around a constant value x_0. Under these conditions, $P(t)=k\langle X\rangle^2e^{-k\langle X\rangle^2t}$, where the average width is $\langle X(t)\rangle=[x_0e^{-t/\eta}+(x_0-f/\kappa)(1-e^{-t)/\eta})]\Theta(f_c-f)+x_1\Theta(f-f_c)$ [Heaviside step function $\Theta(x)$ accounts for the excluded volume interactions at a critical force f_c].

Theory quantitatively explains force dependence of A:a bond lifetimes. A fit of the theoretical predictions of $\langle\tau\rangle$ vs. f calculated with the FB model to experimental data (Fig. 2*B*) showed very good agreement (Fig. 5). The model has five parameters [friction was set to $\zeta=10^{-3}$ pN nm^{-1}s (diffusion of amino acids in water)]: interface stiffness κ=16.7 pN/nm, force-free interface width $x_0=2.8$ nm (in state LR_1), minimal interface width (in LR_2) $x_1=0.6$ nm, escape rate constant $k_0=0.11$ nm^{2}s^{-1}, and transition distance $\sigma_y=0.25$ nm. Of these, κ, x_0, and x_1 can be directly accessed in the simulations, which reveal: $\kappa=10-30$ pN/nm, $x_0=2.0-2.8$ nm, and $x_1=0.5-0.9$ nm. The critical force $f_c\approx33$ pN agrees well with the experimental 30- to 35-pN range (Fig. 5), thus justifying the proposed mechanisms for the catch bond. With these parameters, the distributions of bond

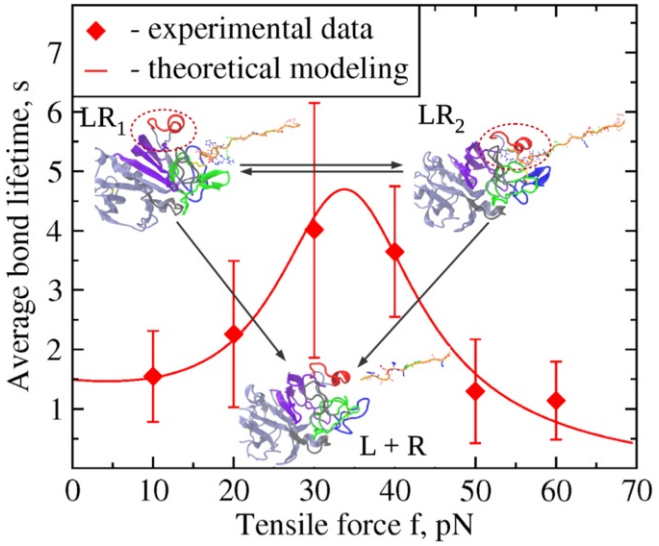

Fig. 5. Catch–slip force response of A:a knob-hole bond. The nonmonotonic behavior of the average bond lifetime $\langle\tau\rangle$ as a function of tensile force f (Fig. 2) is modeled by using FB theory. Snapshots show evolution of the A:a knob-hole complex from the low-affinity bound state LR_1 populated at low forces ($f<10$ pN) to the high-affinity bound state LR_2 stabilized at higher forces ($f\approx30$–35 pN).

lifetimes $P(t)$ compare well with nonparametric density profiles of experimental $P(t)$ for $f = 10$–40 pN (*SI Appendix*, Fig. S3).

Discussion

Using single-molecule experiments, simulations, and theory, we have revealed the structural basis of catch–slip dynamics of forced rupture of A:a knob-hole bonds—the strongest noncovalent interactions in fibrin polymerization (Fig. 1). Control experiments confirmed that the catch–slip behavior was due to dissociation of single knob-hole bonds (Fig. 2). The catch–slip transition was enhanced when both knobs 'A' and 'B' were exposed (Fig. 2). In the presence of 3 mM Ca^{2+}, the A:a bond weakened, and the catch-bond behavior was suppressed.

The movable flap is a molecular force sensor, which triggers the cross-over from the catch-regime to the slip-regime of bond rupture (Fig. 3). Tension-induced strengthening of the A:a knob-hole bond results from dynamic remodeling of the A:a association interface, due to the movable flap translocation, and hole 'a' closing (Fig. 4). Additional evidence for this mechanism came from crystal structures of fibrin(ogen), which showed large-amplitude structure alterations in the movable flap upon Ca^{2+} binding (Fig. 4*E* and *SI Appendix*, Fig. S7). Asp and Gly in the movable flap coordinate Ca^{2+}, and the flap translocation is blocked, which explains the absence of a catch-regime in 3 mM $CaCl_2$ solution. Obtaining recombinant fibrinogen mutants in amounts necessary for single-molecule assays is not feasible. We reconstituted in silico fibrinogen variants with constrained movable flap and with mutation γAsp301His in the movable flap (Finland P21; *SI Appendix*, section S6), which leads to hypofibrinogenemia associated with thrombosis (27). Low 60- to 90-pN rupture forces were observed, which correspond to bond dissociation from the low-affinity bound state LR_1 (*SI Appendix*, Fig. S6).

Several models of catch-bond exist (28), but none account for the binding interface remodeling. We extended the FB model (21, 23, 24, 29) to capture the flap translocation and hole 'a' closure (Fig. 4). These observations were mapped into a mathematical framework, which provides evidence for a multitude of high-affinity bound states. Very good agreement between experimental data and theoretical curves of the $P(t)$ (*SI Appendix*, Fig. S3) and $\langle\tau\rangle$ (Fig. 5) validated the model. FB theory helps: (*i*) to quantify dynamic structural changes at the interface of coupled biomolecules (conformational fluctuations of the binding pocket); (*ii*) to describe friction and temperature dependence of bond rupture (through stochastic differential equation; *SI Appendix*, Eq. S7); and (*iii*) to map the free energy landscape (escape rate and transition state distance). From FB theory, the difference in binding energies for LR_1 and LR_2 is $\Delta\Delta G = -(\kappa/2)(x_0 - x_1)^2 = -5.9$ kcal/mol.

For the A:a bond, $K_d = 5.8$ μM. Assuming that LR_2 is not populated in solution assays, the binding energy for LR_1 is $\Delta G = -7.1$ kcal/mol. From pulling simulations, the work to rupture the A:a bond, estimated by integrating over the force(F)-distance(X) curve, is −5.1 kcal/mol, and assuming near-equilibrium, $\Delta G = -5.1$ kcal/mol. ΔG can also be estimated by counting the total number of disrupted binding contacts $N \times 0.75$ kcal/mol (energy/contact averaged over nonpolar, polar, electrostatic contacts, and hydrogen bonds). For LR_1, $N = 15$ and $\Delta G = -11.2$ kcal/mol. Hence, the experimental −7.1-kcal/mol value for state LR_1 is in the −(5.1–11.2) kcal/mol range from simulations. For LR_2, $\Delta G = -(12.4$–$18.7)$ kcal/mol. Hence, the binding free-energy difference between the catch- and slip-bond is $\Delta\Delta G = -(7.3$–$7.5)$ kcal/mol, which is close to the −5.9 kcal/mol from FB theory.

Our results on the effects of Ca^{2+} on the A:a bond are consistent with the effects of Ca^{2+} on clotting. Calcium ions shorten the clotting time at lower Ca^{2+} levels (30), but at higher Ca^{2+} concentrations, fibrin polymerization is slowed (31). Binding of the knob-A mimetic GPRP peptide interferes with Ca^{2+} binding (32). GPRP inhibits fibrin at $[Ca^{2+}] = 10^{-3}$ M, but the inhibition is abolished at $[Ca^{2+}] = 10^{-5}$ M, because the A:a bonds are stronger at low Ca^{2+} levels (33). The exposure of knobs A and formation of the initial A:a knob-hole bonds precede Ca^{2+} uptake by fibrin, implying that a Ca^{2+}-free medium is favorable for the initiation of fibrin formation (34). The physiological relevance of the A:a knob-hole bonds in the absence of Ca^{2+} is reinforced by the fact that at the site of clotting, the local $[Ca^{2+}]$ might be low due to strong Ca^{2+} uptake by activated platelets (35). Because platelet aggregation at the site of clotting precedes fibrin formation, low $[Ca^{2+}]$ might promote formation of the incipient fibrin clot by enhancing the A:a knob-hole interactions via catch-bonds under the forces of blood flow. In a more general context, our data support the notion that Ca^{2+} can modulate fibrin formation both kinetically and thermodynamically and that the low-affinity Ca^{2+}-binding sites in fibrin might be a part of a physiological regulatory system of blood clot formation.

Functionally, the catch-bond behavior lends shear-enhanced strengthening to the A:a knob-hole bonds that favors fibrin polymerization and prevents damage of stressed clots. This is important early on during fibrin formation, when the incipient clot is small and the hydrodynamic shear stress is in the range that strengthens the knob-hole bonds. The catch-bond mechanism could also help to prevent embolization (clot rupture), during which thrombi lodge in smaller vessels, causing ischemic strokes, for example. The catch-bond mechanism is relevant for all hemostatic clots and pathological thrombi since fibrin is their structural basis. The discovery of the catch bond in fibrin is an important mechanochemical aspect of fibrin structure–function, which advances our understanding of blood clotting.

Materials and Methods

Optical Trap. Our model system is based on an optical trap (*SI Appendix*, Fig. S1) that uses a focused laser beam to generate the piconewton force to hold and move microscopic particles, such as micrometer-size polystyrene beads (5, 36–40). A custom-built optical trap described in ref. 38 was used to measure the mechanical strength of protein–protein complexes subject to a constant tensile force. The core of the optical trapping system was an AxioObserver Z1 inverted microscope and a 60× 1.3-NA Fluor lens combined with a FCBar Nd:YAG laser ($\lambda = 1{,}064$ nm) with 4-W power in continuous TEM-00 mode. A computer-operated 2D acousto-optical deflector was used to control the trap position. The force exerted by the trap on the bead displaced by an amount Δz was measured with a quadrant detector, and the trap position was corrected with an electronic feedback loop to keep the force constant. This system enabled control of the duration of compressive contact between interacting surfaces T, the magnitude of compressive force f_c and the magnitude of the tensile force $f = k_{opt}\Delta z$ (k_{opt}, optical trap stiffness). The time required to separate surface-attached proteins (bond lifetime) τ was measured. Experiments were conducted with the average trap stiffness of $k_{opt} = 0.19 \pm 0.02$ pN/nm. Force calibration and trap stiffness were confirmed with the Stokes' force method. LabVIEW software was used to record laser beam deflection, move the piezoelectric stage, and analyze data off-line.

Measurements of Protein–Protein Interactions. Surface modification and protein preparation are described in *SI Appendix*, section S1. Experiments were performed at room temperature in 20 mM Hepes (pH 7.4) containing 150 mM NaCl, 2 mg/mL BSA, and 0.1% (vol/vol) Triton X-100 added to reduce nonspecific interactions. Some experiments were carried out in the same buffer but with the addition of 3 mM $CaCl_2$. A total of 1 μL of the Fg-coated or fragment D-coated bead suspension (10^7 beads per mL) was added to 50 μL of the working buffer and flowed into a chamber containing pedestals with immobilized fibrin or fragment E on their surface. After the chamber was placed on the microscope stage, a single bead was trapped, and the stage was moved manually to bring a pedestal within 1–2 μm of the trapped bead. After starting the bead oscillation, the separation of the pedestal and the bead was then reduced until they touched each other repeatedly with a

compressive force $f_{comp} = 20$–30 pN and contact duration $T = 0.5$ s. The constant pulling force was varied from $f = 5$–60 pN. Trap displacement signals were recorded at 2,000 scans per second, and a bond lifetime was measured for each pedestal–bead-touching event. Several tens of pedestal–bead pairs were analyzed for each set of conditions. The binding–unbinding events from individual files were summarized; the total number of bond lifetime values recorded for each set of experimental conditions varied from ~3,000 to ~4,500. The bond lifetimes <0.5 s represented nonspecific interactions and were not susceptible for specific inhibition. These short bond lifetimes were not included into data analysis and modeling.

Dynamic Force Measurement of the A:a Bond Rupture in Silico. The atomic structure of the A:a knob-hole complex is described in *SI Appendix*, section S3. We used all-atom Molecular Dynamics simulations on a GPU using the Solvent Accessible Surface Area model of implicit solvation with the CHARMM19 force field (41). We used a lower damping coefficient $\gamma = 3.0$ ps^{-1} for faster system equilibration and efficient sampling of the conformational space (42). In force-ramp simulations, we used time-dependent pulling force $f(t) = k_{opt}(\nu_f t - \Delta x)$, where $\nu_f = 10^3$ μm/s is the virtual pulling speed, $k_{opt} = 100$ pN/nm is the trap spring constant, and Δx is the displacement of a pulled residue. In force-clamp runs, we used constant tensile force $f = 30$–80 pN (Fig. 1*G*). We constrained the C_α-atoms of γLys159 and tagged the C_α-atom of αCys36 (Fig. 1*G*).

ACKNOWLEDGMENTS. We thank Dr. Henry Shuman, who built the optical trap instrument with force-clamp modification, for his help with experiments, data processing, and analysis; and Andrey Mekler for technical assistance. This work was supported by NSF Grant DMR 1505316 (to J.W.W. and V.B.); American Heart Association Grant-in-Aid 13GRNT16960013 (to V.B. and J.W.W.); NIH Grants UO1 HL116330 and RO1 HL135254 (to J.W.W.); Russian Foundation for Basic Research Grants 15-01-06721 (to A.Z.) and 14-04-32066 (to O.K.); Russian Science Foundation Grant 17-71-10202 (to A.Z.); the Program for Competitive Growth at Kazan Federal University; National Institutes of Health Grant R01 GM089685 (to D.T.); and Collie-Welch Chair F-0019 (to D.T.).

1. Weisel JW, Litvinov RI (2017) Fibrin formation, structure and properties. *Subcell Biochem* 82:405–456.
2. Zhmurov A, et al. (2016) Structural basis of interfacial flexibility in fibrin oligomers. *Structure* 24:1907–1917.
3. Yee VC, et al. (1997) Crystal structure of a 30 kDa C-terminal fragment from the γ-chain of human fibrinogen. *Structure* 15:125–138.
4. Kononova O, et al. (2013) Molecular mechanisms, thermodynamics, and dissociation kinetics of knob-hole interactions in fibrin. *J Biol Chem* 288:22681–22692.
5. Litvinov RI, Gorkun OV, Owen SF, Shuman H, Weisel JW (2005) Polymerization of fibrin: Specificity, strength, and stability of knob-hole interactions studied at the single-molecule level. *Blood* 106:2944–2951.
6. Litvinov RI, Weisel JW (2013) Shear strengthens fibrin: The knob–hole interactions display 'catch-slip' kinetics. *J Thromb Haemost* 11:1933–1935.
7. Marshall BT, et al. (2003) Direct observation of catch bonds involving cell-adhesion molecules. *Nature* 423:190–193.
8. Rakshita S, Zhang Y, Manibog K, Shafraza O, Sivasankar S (2012) Ideal, catch, and slip bonds in cadherin adhesion. *Proc Natl Acad Sci USA* 106:18815–18820.
9. Kong F, Garcia AJ, Mould AP, Humphries MJ, Zhu C (2009) Demonstration of catch bonds between an integrin and its ligand. *J Cell Biol* 185:1275–1284.
10. Sauer MM, et al. (2016) Catch-bond mechanism of the bacterial adhesin FimH. *Nat Commun* 7:10738.
11. Yago T, et al. (2006) Platelet glycoprotein Ibα forms catch bonds with human WT vWF but not with type 2B von Willebrand disease vWF. *J Clin Invest* 118:3195–3207.
12. Feghhi S, et al. (2016) Glycoprotein Ib-IX-V complex transmits cytoskeletal forces that enhance platelet adhesion. *Biophys J* 111:601–608.
13. Akiyoshi B, et al. (2010) Tension directly stabilizes reconstituted kinetochore-microtubule attachments. *Nature* 468:576–579.
14. Rai AK, Rai A, Ramaiya AJ, Jha R, Mallik R (2013) Molecular adaptations allow dynein to generate large collective forces inside cells. *Cell* 152:172–182.
15. Huang DL, Bax NA, Buckley CD, Weis WI, Dunn AR (2017) Vinculin forms a directionally asymmetric catch bond with F-actin. *Science* 357:703–706.
16. Barsegov V, Thirumalai D (2005) Dynamics of unbinding of cell adhesion molecules: Transition from catch to slip bonds. *Proc Natl Acad Sci USA* 102:1835–1839.
17. Barsegov V, Thirumalai D (2006) Dynamic competition between catch and slip bonds in selectins bound to ligands. *J Phys Chem B* 110:26403–26412.
18. Lou J, Zhu C (2007) A structure-based sliding-rebinding mechanism for catch bonds. *Biophys J* 92:1471–1485.
19. Chakrabarti S, Hinczewski M, Thirumalai D (2014) Plasticity of hydrogen bond networks regulates mechanochemistry of cell adhesion complexes. *Proc Natl Acad Sci USA* 111:9048–9053.
20. Pereverzev YV, Prezhdo OV, Forero M, Sokurenko EV, Thomas WE (2005) The two-pathway model for the catch-slip transition in biological adhesion. *Biophys J* 89:91446–91454.
21. Zwanzig R (1992) Dynamical disorder: Passage through a fluctuating bottleneck. *J Chem Phys* 97:3587–3589.
22. Everse S, Spraggon G, Veerapandian L, Doolittle R (1999) Conformational changes in fragments D and double-D from human fibrin (ogen) upon binding the peptide ligand Gly-His-Arg-Pro-amide. *Biochemistry* 38:2941–2946.
23. Barsegov V, Chernyak V, Mukamel S (2002) Multitime correlation functions for single molecule kinetics with fluctuating bottlenecks. *J Chem Phys* 116:4240–4251.
24. Hyeon C, Hinczewski M, Thirumalai D (2014) Evidence of disorder in biological molecules from single molecule pulling experiments. *Phys Rev Lett* 112:138101.
25. Hyeon C, Thirumalai D (2007) Measuring the energy landscape roughness and the transition state location of biomolecules using single molecule mechanical unfolding experiments. *J Phys Condens Matter* 19:113101.
26. Bell GL (1978) Models for the specific adhesion of cells to cells. *Science* 200:618–627.
27. Asselta R, et al. (2015) Clinical and molecular characterisation of 21 patients affected by quantitative fibrinogen deficiency. *Thromb Haemost* 114:567–576.
28. Thomas W, Vogel V, Sokurenko E (2008) Biophysics of catch bonds. *Annu Rev Biophys* 37:399–416.
29. Bicout DJ, Szabo A (1998) Escape through a bottleneck undergoing non-Markovian fluctuations. *J Chem Phys* 108:5491–5497.
30. Brass E, Forman W, Edwards R, Lindan O (1978) Fibrin formation: Effect of calcium ions. *Blood* 52:654–658.
31. Haeberli A, Straub P, Dietler G, Kaenzig W (1987) The influence of calcium ions on fibrin polymerization. *Biopolymers* 26:27–43.
32. Laudano A, Doolittle R (1981) Influence of calcium ion on the binding of fibrin amino terminal peptides to fibrinogen. *Science* 212:457–459.
33. Furlan M, Rupp C, Beck E (1983) Inhibition of fibrin polymerization by fragment D is affected by calcium, Gly-Pro-Arg and Gly-His-Arg. *BBA Prot Struct* 742:25–32.
34. Mihalyi E (1988) Clotting of bovine fibrinogen. Calcium binding to fibrin during clotting and its dependence on release of fibrinopeptide B. *Biochemistry* 27:967–976.
35. Varga-Szabo D, Braun A, Nieswandt B (2009) Calcium signaling in platelets. *J Thromb Haemost* 7:1057–1066.
36. Litvinov RI, Shuman H, Bennett JS, Weisel JW (2002) Binding strength and activation state of single fibrinogen-integrin pairs on living cells. *Proc Natl Acad Sci USA* 99:7426–7431.
37. Litvinov RI, Bennett JS, Weisel JW, Shuman H (2005) Multi-step fibrinogen binding to the integrin αIIbβ3 detected using force spectroscopy. *Biophys J* 89:2824–2834.
38. Litvinov RI, et al. (2011) Dissociation of bimolecular αIIbβ3-fibrinogen complex under a constant tensile force. *Biophys J* 100:165–173.
39. Litvinov RI, et al. (2012) Resolving two-dimensional kinetics of receptor-ligand interactions using binding-unbinding correlation spectroscopy. *J Biol Chem* 287:35272–35285.
40. Litvinov RI, Farrell DH, Weisel JW, Bennett JS (2016) The platelet integrin αIIbβ3 differentially interacts with fibrin versus fibrinogen. *J Biol Chem* 291:7858–7867.
41. Ferrara P, Apostolakis J, Caflisch A (2002) Evaluation of a fast implicit solvent model for molecular dynamics simulations. *Proteins* 46:24–33.
42. Zhmurov A, et al. (2012) Mechanical transition from α-helical coiled coils to β-sheets in fibrin(ogen). *J Am Chem Soc* 134:20396–20402.